Journal of Materials Chemistry A

Accepted Manuscript

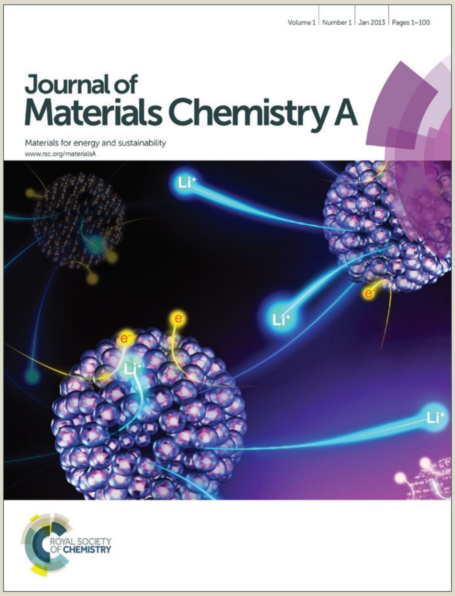

ROYAL SOCIETY OF CHEMISTRY

www.rsc.org/materialsA

Synthesis and Electrochemical Properties of $Li_3V_2(P_{1-x}B_xO_4)_3/C$ Cathode Materials

Kai Feng,[a*] **Yi Cheng,**[a,b] **Meiri Wang,**[a] **Hongzhang Zhang,**[a] **Xianfeng Li,**[a,c] **Huamin Zhang**[a,c*]

B-doped compounds $Li_3V_2(P_{1-x}B_xO_4)_3/C$ (x = 0, 0.01, 0.03, 0.07) are prepared by a sol-gel method. The crystal structure, morphology and electrochemical properties of B-doped $Li_3V_2(PO_4)_3$ are investigated. X-ray diffraction (XRD) analysis indicates that B atom enters the crystal structure of $Li_3V_2(PO_4)_3$ but does not change the monoclinic structure. Cycle stability and rate performances measurements reveal that moderate B doping improves the electrochemical properties of $Li_3V_2(PO_4)_3$. Among all the B-doped samples, $Li_3V_2(P_{0.97}B_{0.03}O_4)_3/C$ shows the largest initial discharge capacity, best cycle stability and rate performances. In the potential range 3.0-4.3 V, $Li_3V_2(P_{0.97}B_{0.03}O_4)_3/C$ delivers the discharge capacity of 127.5 mAh/g at 0.2 C rate, while at 20 C the discharge capacity remains above 100 mAh/g. After 100 cycles, the discharge capacity retention is 98%. Moreover, electrochemical impedance spectroscopy (EIS) and cyclic voltammetry (CV) curves indicate that B doping not only decreases the charge transfer resistance but increases the Li-ion diffusion rate.

---

[a] *Division of energy storage, Dalian National Laboratory for Clean Energy, Dalian Institute of Chemical Physics, Chinese Academy of Sciences, Zhongshan Road 457, Dalian, 116023, China.*

[b] *University of Chinese Academy of Sciences, Beijing, 100039, China*

[c] *Collaborative Innovation Center of Chemistry for Energy Materials (iChEM), Dalian 116023 (P.R. China)*

The excellent electrochemical performance of $Li_3V_2(P_{0.97}B_{0.03}O_4)_3/C$ can be attributed to its larger Li ion diffusion, smaller particle size, higher structural stability and electronic conductivity induced by B doping.

Introduction

With urgent requirements of large-scale energy storage, hybrid electric vehicles (HEVs) and electric vehicles (EVs), rechargeable lithium ion batteries (LIB) have been extensively researched. Polyanion compounds, a kind of LIB cathode materials that possess high thermal stability, long-term structure stability and higher working voltage, have attracted worldwide interests since the discovery of the electrochemically active $LiFePO_4$.[1-9] A large number of phosphates cathode materials, such as $LiMnPO_4$,[10] Li_2FePO_4F,[11] and $Li_3V_2(PO_4)_3$[12-14] have been extensively studied. Monoclinic $Li_3V_2(PO_4)_3$ (LVP) is one of the most investigated compounds for its high energy and power density, thermal stability, and excellent electrochemical property at low temperature. However, the low electrical conductivity (10^{-8} S cm^{-1}) and instability working between 3.0-4.8 V limits not only complete utilization of its theoretical capacity but high rate performances.[15] To overcome these problems, ion-doping, conductive materials coatings, particle size reducing and morphology tailoring have been explored.[8]

Ion-doping is the most expediently method and can improve the intrinsic electronic conductivity and Li-ion diffusion. Numberless of ions with different ion radius and oxidation states have been doped into the Li or/and V sites. With Fe^{3+}, Cr^{3+},

Ce^{3+}, Zn^{2+}, Mg^{2+}, Ni^{2+}, Co^{2+}, $Zr^{4+}$and Ti^{4+} partly replacing the V^{3+} ion, the capacity, cycling stability, electronic conductivity or Li^+ ion diffusion properties can be improved significantly.[8, 16-24] Yang et al synthesized Zn-doped $Li_3V_{2-x}Zn_x(PO_4)_3$ (x = 0, 0.02, 0.04, 0.06) cathode materials and found that $Li_3V_{1.96}Zn_{0.04}(PO_4)_3$ possesses the highest electronic conductivity, initial discharge capacity of 105.5 mAh/g at 5C and better capacity retention property than the primary LVP.[25] Besides, doping Na^+, Ca^{2+} cations in the Li site also enhances the electrochemistry properties of LVP.[26, 27] Chen et al use the dopant of Na^+ with larger ionic radius to improve the Li^+ diffusion with three times by broadening the Li^+ transportation channels of the crystal structures.[27] In addition, doping at two different sites simultaneously or at the same sites with different cations were studied as well. For example, $Li_{2.5}Na_{0.5}V_{(2-2x/3)}Ni_x(PO_4)_3$[28] and $Li_3V_{1.9}Ti_{0.05}Mn_{0.05}(PO_4)_3$[29] were both explored and the electrochemical properties were partly enhanced. On the contrast, there are few reports about anion doping, especially at P site. Only Cl^- and F^- anions have been researched to substitute the entire $(PO_4)^{3-}$ group, which has positive effect on the electrochemical properties.[30, 31] The chlorine-doped $Li_3V_2(PO_4)_3$ sample possessed higher ionic, electronic conductivity, and better cycling stability.[31]

Due to the lighter atom weight of B than P, borate could induce higher theory capacity than phosphate. In addition, as proved in $LiFePO_4$,[32, 33] B doping can inhibit the crystal growth, which reduces the particle size. In addition, the weaker B-O bond than P-O bond can provide borate larger Li^+ diffusion. At the same time, B doping makes the PO_4 octahedral distorted, which can decrease the band gap of phosphate and thus increase the electronic conductivity. Last but not least, the differences of B-O and P-O bonds buffer the deformation of $Li_3V_2(PO_4)_3$ host crystals and improve the structural stability. So the B-doping on the P sites could enhance the electrochemical properties of phosphate.

In this work, we prepared B doped $Li_3V_2(P_{1-x}B_xO_4)_3$/C (x = 0, 0.01, 0.03, 0.07) samples via sol-gel method and post-thermal process. And the phase composition, microstructure, and electrochemical performance of the cathode materials are investigated.

Experimental

Synthesis of $Li_3V_2(P_{1-x}B_xO_4)_3$/C

The $Li_3V_2(P_{1-x}B_xO_4)_3$/C (x = 0, 0.01, 0.03, 0.07) samples were synthesized via a sol–gel method with LiOH, NH_4VO_3, $NH_4H_2PO_4$, H_3BO_3 and oxalic acid as raw materials in the molar ratio of 3:2:(3-3x):3x:3. Oxalic acid was used here as a chelating reagent and reducing agent simultaneously. In addition, sucrose powders with 20 wt% of $Li_3V_2(P_{1-x}B_xO_4)_3$ were used as the source of carbon coating on the surface of the materials. Firstly, oxalic acid and NH_4VO_3 were dissolved in deionized water with magnetic stirring at 80 ^oC. After a clear blue solution formed, stoichiometric of $NH_4H_2PO_4$, H_3BO_3, LiOH, and sucrose with 20 wt% of $Li_3V_2(P_{1-x}B_xO_4)_3$ were added to the solution and kept on stirring until a blue sol was formed, then the gel was obtained in an air oven at 80 °C. The gel was grinded to powder and heated at 350 ^oC in a tube furnace under a flowing Ar atmosphere for 5 h to expel H_2O and NH_3. Finally, the resulting powder was reground and sintered at 750 ^{o}C for 15 h in an argon atmosphere and the final samples were obtained.

Materials Characterization

The phase analysis of the samples was performed using a PANalytical powder X-ray diffraction with monochromatic Cu Kα radiation at λ=1.54Å in the 2θ range of 10-70°. Thermogravimetric analysis (TGA, PYRIS Diamond TG-DTA, High Temp 115) was conducted under flowing air at a heating rate of 10 ^{o}C/min from 30 ^{o}C to 600 ^{o}C. The morphology of the samples was investigated by field scanning electron microscope (SEM, JOE7800) working at 15kV.

Electrochemical Measurements

The electrochemical properties were tested with CR2016 coin cells assembled in a glove box filled with pure argon gas. The cathodes were prepared by mixing the prepared LVP samples, Super P, and polyvinylidene fluoride in a weight ratio of 7:2:1 dissolved in N-methyl pyrrolidone to form slurry, which was uniformly coating on an Al foil and dried in vacuum at 120 °C. Metallic lithium foil was used as the anode electrode, Celgard 2325 membrane was used as a separator and 1M $LiPF_6$ in ethylene carbonate and dimethyl carbonate (1:1 volume.) was used as electrolyte. Galvonostatic charge−discharge measurement was performed in the voltage window of 3.0−4.3 V and 3.0−4.8 V respectively on LAND 2100 system (Wuhan, China). Cyclic voltammetry (CV) curves were recorded from 3.0−4.3 V vs. Li^+/Li by CHI electrochemical working station at 25 ^{o}C. Electrochemical impedance spectroscopy (EIS) of the batteries were measured in a frequency range of 100 KHz to 0.1 Hz using a Salarton 1287 test system with perturbation amplitude of 5 mV under open circuit potential conditions.

Results and Discussion

Material Characterization

Figure 1a presents the X-ray diffraction (XRD) patterns of $Li_3V_2(P_{1-x}B_xO_4)_3/C$ (x = 0, 0.01, 0.03, 0.07) samples. The XRD patterns of all the samples coincide with the standard one, which suggests that B doping did not change the monoclinic crystal structure of $Li_3V_2(PO_4)_3$. Figure 1b reveals that with more B being incorporated, the peak shifting to right side becomes larger. It indicates that the cell size of LVP crystals compresses as a result of smaller B incorporation according to Bragg formula and proves the B indeed interspaced the P sites as expected.

The morphology of $Li_3V_2(P_{1-x}B_xO_4)_3/C$ (x = 0, 0.01, 0.03, 0.07) samples are shown in Figure 2, from which it can be clearly observed that the samples are severely agglomerated. The samples are comprised of globular particles and a few of needle-like strips. The particle size of the B-doped samples varies with different B content and smaller than the pure $Li_3V_2(PO_4)_3/C$ sample. As more B is incorporated, the particles grow smaller firstly then larger. And the sample with 3 mol% B doping possesses the smallest particle size because that moderate B doping inhibits the growth of LVP crystal, while excess B may decrease the crystallizing point and promote the growth of LVP crystal. The smaller particle size is beneficial to the electrochemical performances.

As shown in Figure 3, the carbon contents of the samples are investigated by thermogravimetric analysis. The weight loss before 300 ^{o}C is attributed to the evaporation of absorbed and chemically bonded water in the samples. The abrupt weight loss between 300 ^{o}C-500 ^{o}C is due to the combustion of residual carbon. The carbon content of $Li_3V_2(P_{1-x}B_xO_4)_3/C$ for x = 0, 0.01, 0.03, and 0.07 is 2.7%, 2.8%, 2.3%, and 3.1%, respectively. TEM was measured to confirm the presence of a carbon layer on the surface of $Li_3V_2(P_{1-x}B_xO_4)_3$. As shown in Figure 2b, a carbon layer with thickness of about 3-5 nm is found to coating on the surface of $Li_3V_2(P_{0.97}B_{0.03}O_4)_3/C$, which makes contribution to improving the electronic conductivity in the interstitial particle/ boundary region.

Electrochemical Performances

Charge-discharge studies were performed between 3.0-4.3 V and 3.0-4.8 V at 0.2 C. As shown in Figure 4, all the samples present three and four stages of lithium extraction and insertion between 3.0-4.3 V and 3.0-4.8 V respectively, which indicates that the $Li_3V_2(PO_4)_3$ was successfully synthesized and the B doping did not destroy the crystal structure of $Li_3V_2(PO_4)_3$, consisting with the XRD results. During charging, the first Li (1 mol of Li) is extracted in two-step at 3.6 V ($Li_{2.5}V_2(PO_4)_3$) and 3.7 V ($Li_2V_2(PO_4)_3$), while the removing of the second Li occurred at 4.1 V vs. Li^+ with a long distinct plateau.[8] The above three distinct plateau regions correspond to the

V^{3+}/V^{4+} redox couple. The final third Li is extracted at 4.55 V vs. Li^+ to form $V_2(PO_4)_3$ with mixed valance states V^{4+} and V^{5+}. However, during discharging, the first two Li insertion occurres at 4.10 V reversibly with a monotonic curve followed by two distinct plateaus at 3.7 and 3.6 V. As shown in Fig.4, with the increasing of doped B, the initial discharge specific capacity firstly increases and then decreases. The initial discharge specific capacity are 116.8, 120.9, 127.5, 124 mAh g^{-1} between 3.0-4.3 V and 154.9, 162, 175.7, 158.2 mAh g^{-1} between 3.0-4.8 V for samples with x = 0, 0.01, 0.03, 0.07, respectively. As discussed above, the particle size reduction and electronic conductivity enhancement can improve the reaction area and the utilization of active materials, which is beneficial to increase the initial capacity. In addition, lighter atom weight of B atom than P atom brings larger initial capacity. However, when doping content excesses the optimum value, the excess B enlarged the particle size and generates inactive materials, depressing the initial capacity.

Figure 5 reveals the cycle stability of the $Li_3V_2(P_{1-x}B_xO_4)_3/C$ (x = 0, 0.01, 0.03, 0.07) samples in the range of 3.0~4.3 V and 3.0~4.8 V. After 100 cycles, the discharge capacity retentions are 94.3%, 96.4%, 98.0% and 91.0% between 3.0-4.3 V and 79.7%, 78.8%, 81.8 and 71.8% between 3.0-4.8 V for x = 0, 0.01, 0.03, 0.07, respectively, which indicates that the sample with x = 0.03 possesses the best cycle stability. This is because that with different ion radius to P atom, B doping makes the PO_4 tetrahedra distorted and can buffer the deformation of $Li_3V_2(PO_4)_3$ host crystals and improve the structural stability. In addition, B atom can be coordinated to four or three O atoms, which is also useful to buffer the deformation of $Li_3V_2(PO_4)_3$ host crystals during charging and discharging.

Figure 6 shows rate performances of all samples at 0.2 C, 0.5 C, 1 C, 2 C, 5 C, 10 C, 20 C (only 3.0-4.3 V) and 0.2 C, respectively. Between both 3-4.3 V and 3-4.8 V, the 3 mol% B-doped sample exhibits evident larger capacity than the pure $Li_3V_2(PO_4)_3$. For each sample, the discharge capacity decreases with increasing current density. The $Li_3V_2(P_{0.97}B_{0.03}O_4)_3/C$ sample displays the best rate performance, showing remarkably improved rate capability at higher rates, delivering a discharge capacity as high as 100 mAh g^{-1} even at 20 C.

To find the reason why the electrochemical properties of B doping samples are improved greatly, the kinetic properties of $Li_3V_2(P_{1-x}B_xO_4)_3/C$ (x = 0, 0.01, 0.03, 0.07) were further investigated by EIS analysis and CV curves. A semicircle and a sloping line can be obviously observed from the Nyquist plots (Figure 7a) of all $Li_3V_2(P_{1-x}B_xO_4)_3/C$ (x = 0, 0.01, 0.03, 0.07) samples. In EIS spectra, the charge transfer resistance estimated from the semicircle in high-middle frequency region is linked to the charge transfer process. And the numerical value of the diameter of the semicircle on the Z' axis is approximated as the charge transfer resistance (Rct). $Li_3V_2(P_{0.97}B_{0.03}O_4)_3/C$ has the lowest charge transfer resistance, which indicates that B doping effectively enhanced the charge transfer by minishing the band gap via making the PO_4 tetrahedra distorted. The sloping line is attributed to the Warburg impedance, which is associated with the diffusion of Li ions. [8, 34, 35] And the diffusion coefficient of Li ions (D) is calculated according to the following Eq. (1) and Eq. (2)

$$D=R^2T^2/2A^2n^4F^4C^2\sigma^2 \qquad (1)$$

$$Z' = R_e + R_{ct} + \sigma\omega^{-1/2} \qquad (2)$$

where R is the gas constant, T is the absolute temperature, A is the surface area of the cathode, n is the number of electrons per molecule during oxidization, F is the Faraday constant, C is the concentration of lithium-ion, σ is the Warburg factor which has a relationship with Z' as shown in Eq. (2), R_e is the resistance between the electrolyte and electrode, R_{ct} is the charge transfer resistance, and ω is angle frequency. [36, 37] Figure 7b shows the relationship between Z' and square root of frequency ($\omega^{-1/2}$) in the low-frequency region. The slope of the linearly fitted lines of Z' and $\omega^{-1/2}$ is Warburg factor (σ). The diffusion coefficient of Li ions (D) can be easily obtained according to Eq. (1). Table 1 presents the values of σ and D. Li ion diffusion coefficient of B-doped samples is about 4×10^{-12} cm^2 S^{-1}, much higher than that of $Li_3V_2(PO_4)_3/C$ (1.0×10^{-12} cm^2 S^{-1}), which indicates that B doping indeed increase the diffusion of Li ion, which is favorable for improving the electrochemical performances.

The CV curves of $Li_3V_2(P_{0.97}B_{0.03}O_4)_3/C$ and the pure $Li_3V_2(PO_4)_3/C$ between 3.0-4.3 V are shown in Figure 8. It can be seen that the $Li_3V_2(P_{0.97}B_{0.03}O_4)_3/C$ possesses smaller distance between oxidation and reduction peaks than pure $Li_3V_2(PO_4)_3/C$, suggesting weaker electrochemical polarization. In addition, the oxidation and reduction peaks of $Li_3V_2(P_{0.97}B_{0.03}O_4)_3/C$ are stronger than $Li_3V_2(PO_4)_3/C$. The peak current density is represented as follows:

$$I_p = 2.6\times10^5 n^{3/2} C_0 D^{1/2} v^{1/2}$$

Where n is the number of electrons transferred per molecule during the intercalation, C_0 is the concentration of lithium ions, D is the diffusion coefficient of Li ions, and v is the scan rate.[38] Since $I_p \propto D^{1/2}$, the diffusion coefficient of Li ions is higher in $Li_3V_2(P_{0.97}B_{0.03}O_4)_3$/C electrode than in the pure $Li_3V_2(PO_4)_3$ /C electrode, which is agreement with the analysis result of EIS. By the analysis of EIS and CV, B-doping effectively enhances the charge transfer and Li ion diffusion, which is one of the most important reasons for the outstanding electrochemical performance of $Li_3V_2(P_{0.97}B_{0.03}O_4)_3$/C.

In all, the greatly improved rate capability and cycle stability of the $Li_3V_2(P_{0.97}B_{0.03}O_4)_3$/C sample can be attributed to four factors. Firstly, the lighter atom weight of B than P atoms provides larger initial discharging capacity. Secondly, the B-doping inhibits the crystal growth of $Li_3V_2(PO_4)_3$ and decreases the particle size, which shorten the Li ion diffusion distances and increase the electrochemical reaction area. In addition, compared with P-O bond, the weaker B-O bond resulting from the B doping also provides larger Li^+ diffusion, which is beneficial to the rate performances. Last but not least, with different ion radius and coordination habit to P atom, B-doping can buffer the deformation of $Li_3V_2(PO_4)_3$ host crystals during charging and discharging and improve the structural stability.

Conclusions

A series of B doped samples $Li_3V_2(P_{1-x}B_xO_4)_3$/C (x = 0, 0.01, 0.03, 0.07) have been successfully synthesized by a sol–gel method. The XRD patterns reveals that B enters into the structure of $Li_3V_2(PO_4)_3$ but does not change the monoclinic structure. SEM images prove that B-doped samples possess smaller particle size than pure $Li_3V_2(PO_4)_3$, which can reduce the Li ion diffusion distance and increase reaction area. B doping significantly improves the specific capacity, rate property and cycling stability of $Li_3V_2(PO_4)_3$. $Li_3V_2(P_{0.97}B_{0.03}O_4)_3/C$ possesses the best rate discharge performance (100 $mAhg^{-1}$@20 C, 3-4.3 V) and cycling performance (98% after 100 cycles, 3-4.3 V). B doping enhances the electrochemical properties for the following reasons: (1) reducing particle size; (2) enhancing the Li ion diffusion and electronic conductivity; (3) enlarging initial specific capacity; (4) improving the structural stability and cycling stability. Here we synthesized the $Li_3V_2(PO_4)_3/C$ with enhanced electrochemical properties by B doping, which provides a promising cathode material $Li_3V_2(P_{0.97}B_{0.03}O_4)_3/C$ for high-power Li rechargeable batteries.

Acknowledgements

The authors greatly acknowledge the financial support from China Natural Science Foundation (Grant Nos. 51403209, 21406221, 21206158, 21476224, 21406219 and 51361135701), Dalian Municipal Outstanding Young Talent Foundation (2014J11JH131).

References

1. S. Y. Chung, J. T. Bloking and Y. M. Chiang, *Nat Mater*, 2002, **1**, 123-128.
2. N. Recham, J. N. Chotard, L. Dupont, C. Delacourt, W. Walker, M. Armand

and J. M. Tarascon, *Nat Mater*, 2010, **9**, 68-74.

3. P. Barpanda, M. Ati, B. C. Melot, G. Rousse, J. N. Chotard, M. L. Doublet, M. T. Sougrati, S. A. Corr, J. C. Jumas and J. M. Tarascon, *Nat Mater*, 2011, **10**, 772-779.
4. G. Hautier, A. Jain, H. Chen, C. Moore, S. P. Ong and G. Ceder, *J. Mater. Chem.*, 2011, **21**, 17147.
5. M. S. Islam, R. Dominko, C. Masquelier, C. Sirisopanaporn, A. R. Armstrong and P. G. Bruce, *J. Mater. Chem.*, 2011, **21**, 9811.
6. R. Tripathi, G. Popov, X. Sun, D. H. Ryan and L. F. Nazar, *J. Mater. Chem. A*, 2013, **1**, 2990.
7. J. M. Clark, C. Eames, M. Reynaud, G. Rousse, J.-N. Chotard, J.-M. Tarascon and M. S. Islam, *J. Mater. Chem. A*, 2014, **2**, 7446.
8. X. Rui, Q. Yan, M. Skyllas-Kazacos and T. M. Lim, *J. Power Sources*, 2014, **258**, 19-38.
9. A. Yamada, M. Hosoya, S. C. Chung, Y. Kudo, K. Hinokuma, K. Y. Liu and Y. Nishi, *J. Power Sources*, 2003, **119**, 232-238.
10. C. Delacourt, P. Poizot, M. Morcrette, J. M. Tarascon and C. Masquelier, *Chem. Mater.*, 2004, **16**, 93-99.
11. T. N. Ramesh, K. T. Lee, B. L. Ellis and L. F. Nazar, *Electrochem. Solid State Lett.*, 2010, **13**, A43-A47.
12. H. Huang, S. C. Yin, T. Kerr, N. Taylor and L. F. Nazar, *Adv. Mater.*, 2002, **14**, 1525.

13. M. Y. Saidi, J. Barker, H. Huang, J. L. Swoyer and G. Adamson, *J. Power Sources*, 2003, **119**, 266-272.

14. S. C. Yin, H. Grondey, P. Strobel, M. Anne and L. F. Nazar, *J. Am. Chem. Soc.*, 2003, **125**, 10402-10411.

15. J. Su, X.-L. Wu, J.-S. Lee, J. Kim and Y.-G. Guo, *J. Mater. Chem. A*, 2013, **1**, 2508-2514.

16. J. N. Son, G. J. Kim, M. C. Kim, S. H. Kim, V. Aravindan, Y. G. Lee and Y. S. Lee, *J. Electrochem. Soc.*, 2012, **160**, A87-A92.

17. S. Zhang, Q. Wu, C. Deng, F. L. Liu, M. Zhang, F. L. Meng and H. Gao, *J. Power Sources*, 2012, **218**, 56-64.

18. G. Bai, Y. Yang and H. Shao, *J. Electroanal. Chem.*, 2013, **688**, 98-102.

19. J. Dang, F. Xiang, N. Gu, R. Zhang, R. Mukherjee, I.-K. Oh, N. Koratkar and Z. Yang, *J. Power Sources*, 2013, **243**, 33-39.

20. W.-l. Wu, J. Liang, J. Yan and W.-f. Mao, *J. Solid State Electrochem.*, 2013, **17**, 2027-2033.

21. J. Yao, S. Wei, P. Zhang, C. Shen, K.-F. Aguey-Zinsou and L. Wang, *J. Alloys Compd.*, 2013, **549**, 375.

22. L. Chen, B. Yan, Y. Xie, S. Wang, X. Jiang and G. Yang, *J. Power Sources*, 2014, **261**, 188-197.

23. M. Y. Hassaan, S. M. Salem and M. G. Moustafa, *J. Non-Cryst. Solids*, 2014, **391**, 6-11.

24. Y. Chen, Y. Zhao, X. An, J. Liu, Y. Dong and L. Chen, *Electrochim. Acta*, 2009,

54, 5844-5850.

25. Y. Yang, W. Xu, R. Guo, L. Liu, S. Wang, D. Xie and Y. Wan, *J. Power Sources*, 2014, **269**, 15-23.
26. C. Sun, S. Rajasekhara, Y. Dong and J. B. Goodenough, *Acs Appl. Mater. Inter.*, 2011, **3**, 3772-3776.
27. Q. Chen, X. Qiao, Y. Wang, T. Zhang, C. Peng, W. Yin and L. Liu, *J. Power Sources*, 2012, **201**, 267-273.
28. W. Wang, Z. Chen, J. Zhang, C. Dai, J. Li and D. Ji, *Electrochim. Acta*, 2013, **103**, 259-265.
29. S. Zhang, Q. Wu, C. Deng, F. L. Liu, M. Zhang, F. L. Meng and H. Gao, *J. Power Sources*, 2012, **218**, 56-64.
30. S. Zhong, L. Liu, J. Liu, J. Wang and J. Yang, *Solid State Commun.*, 2009, **149**, 1679-1683.
31. J. Yan, W. Yuan, Z.-Y. Tang, H. Xie, W.-F. Mao and L. Ma, *J. Power Sources*, 2012, **209**, 251-256.
32. L. Zhang, X. Kang, T. Wumair, J. Dou and Y. Han, *J. Power Sources*, 2013, **243**, 147-151.
33. Z.-G. Ren, M.-Z. Qu and Z.-L. Yu, *J. Inorg. Mater.*, 2010, **25**, 230-234.
34. C. Deng, S. Zhang, S. Y. Yang, Y. Gao, B. Wu, L. Ma, B. L. Fu, Q. Wu and F. L. Liu, *J. Phys. Chem. C*, 2011, **115**, 15048-15056.
35. J. S. Huang, L. Yang, K. Y. Liu and Y. F. Tang, *J. Power Sources*, 2010, **195**, 5013-5018.

36. H. Liu, Q. Cao, L. J. Fu, C. Li, Y. P. Wu and H. Q. Wu, *Electrochem. Commun.*, 2006, **8**, 1553-1557.

37. X. Du, W. He, X. Zhang, Y. Yue, H. Liu, X. Zhang, D. Min, X. Ge and Y. Du, *J. Mater. Chem.*, 2012, **22**, 5960-5969.

38. H. Liu, L. J. Fu, H. P. Zhang, J. Gao, C. Li, Y. P. Wu and H. Q. Wu, *Electrochem. Solid State Lett.*, 2006, **9**, A529-A533.

Figure Captions

Figure 1. (a) XRD patterns of $Li_3V_2(P_{1-x}B_xO_4)_3/C$ (x = 0, 0.01, 0.03, 0.07) samples; (b) Partial enlarged view of the XRD patterns of $Li_3V_2(P_{1-x}B_xO_4)_3/C$ (x = 0, 0.01, 0.03, 0.07)

Figure 2. SEM images of $Li_3V_2(P_{1-x}B_xO_4)_3/C$ samples with different B contents: (a) x = 0, (b) x = 0.01, (c) x = 0.03, (d) x = 0.07.

Figure 3. (a) TGA curves of $Li_3V_2(P_{1-x}B_xO_4)_3/C$ (x = 0, 0.01, 0.03, 0.07) and (b)TEM images of $Li_3V_2(P_{0.97}B_{0.03}O_4)_3/C$

Figure 4. Initial galvanostatic voltage profiles of $Li_3V_2(P_{1-x}B_xO_4)_3/C$ (x = 0, 0.01, 0.03, 0.07) at the cut-off voltage of 3~4.3 V (a) and 3~4.8 V (b).

Figure 5. Cycle performances of $Li_3V_2(P_{1-x}B_xO_4)_3/C$ (x = 0, 0.01, 0.03, 0.07) at the current of 0.2 C in the voltage range of 3~4.3 V(a) and 3~4.8 V(b).

Figure 6. (a) Discharge capacities of the $Li_3V_2(P_{1-x}B_xO_4)_3/C$ (x = 0, 0.01, 0.03, 0.07) samples at the current of 0.2 C, 0.5 C, 1 C, 2 C, 5 C, 10 C, 20 C and 0.2 C in the voltage range of 3~4.3V; (b) 0.2 C, 0.5 C, 1 C, 2 C, 5 C, 10 C and 0.2 C in the voltage range of 3~4.8 V.

Figure 7. (a) Electrochemical impedance spectroscopy (EIS) spectra of the $Li_3V_2(P_{1-x}B_xO_4)_3/C$ (x = 0, 0.01, 0.03, 0.07); (b) Relationship between Z' and $\omega^{-1/2}$ in the low-frequency region.

Figure 8. Cyclic voltammetry profiles of $Li_3V_2(P_{1-x}B_xO_4)_3/C$ (x = 0, 0.03)

Table 1.Kinetic parameters of $Li_3V_2(P_{1-x}B_xO_4)_3$/C (x = 0, 0.01, 0.03, 0.07)

Sample	R_{ct} (Ω)	σ	$D_{Li}{}^{+}$(cm^2 s^{-1})/EIS
$Li_3V_2(PO_4)_3$/C	136.9	34.9	1.0×10^{-12}
$Li_3V_2(P_{1.99}B_{0.01}O_4)_3$/C	113	17.2	4.2×10^{-12}
$Li_3V_2(P_{1.97}B_{0.03}O_4)_3$/C	56.5	18.8	3.6×10^{-12}
$Li_3V_2(P_{1.93}B_{0.07}O_4)_3$/C	133.2	18.0	3.9×10^{-12}

R_{ct}: charge transfer resistance. σ: Warburg factor. $D_{Li}{}^{+}$: diffusion coefficient of Li^+ion.

Figure 1

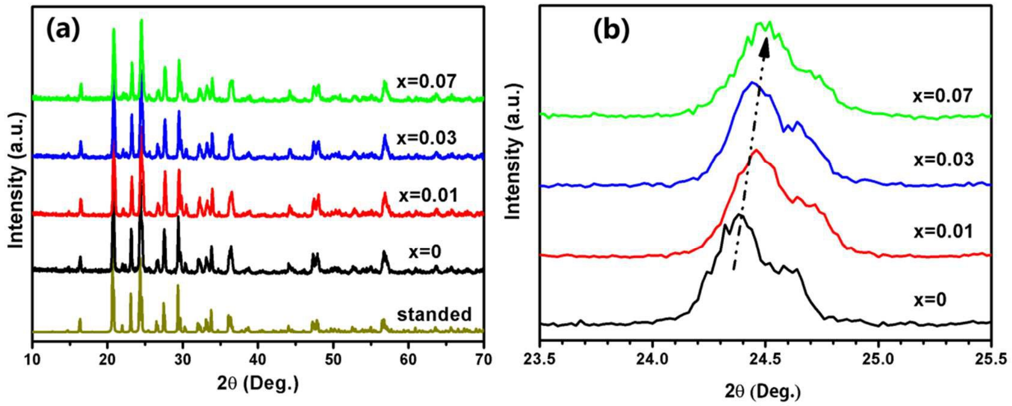
(a)
Intensity (a.u.)
x=0.07
x=0.03
x=0.01
x=0
standed
10
20
30
40
50
60
70
2θ (Deg.)
(b)
Intensity (a.u.)
x=0.07
x=0.03
x=0.01
x=0
23.5
24.0
24.5
25.0
25.5
2θ (Deg.)

Figure 2

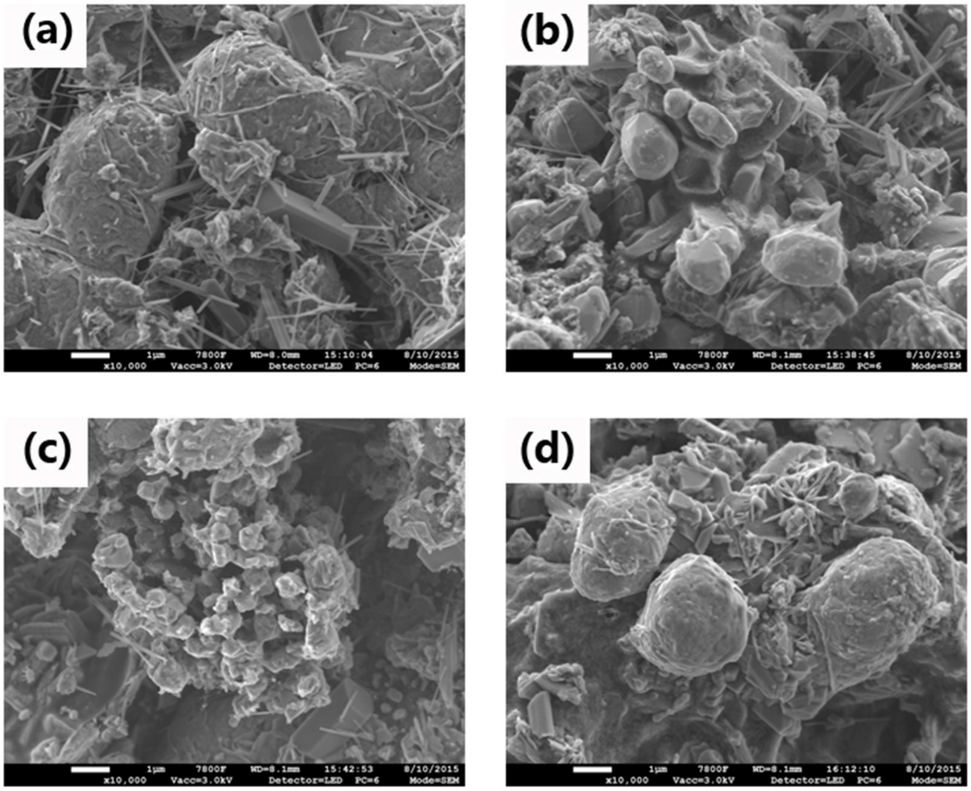
(a)
1μm 7800F WD=8.0mm 15:10:04 8/10/2015
x10,000 Vacc=3.0kV Detector=LED PC=6 Mode=SEM
(b)
1μm 7800F WD=8.1mm 15:38:45 8/10/2015
x10,000 Vacc=3.0kV Detector=LED PC=6 Mode=SEM
(c)
1μm 7800F WD=8.1mm 15:42:53 8/10/2015
x10,000 Vacc=3.0kV Detector=LED PC=6 Mode=SEM
(d)
1μm 7800F WD=8.1mm 16:12:10 8/10/2015
x10,000 Vacc=3.0kV Detector=LED PC=6 Mode=SEM

Figure 3

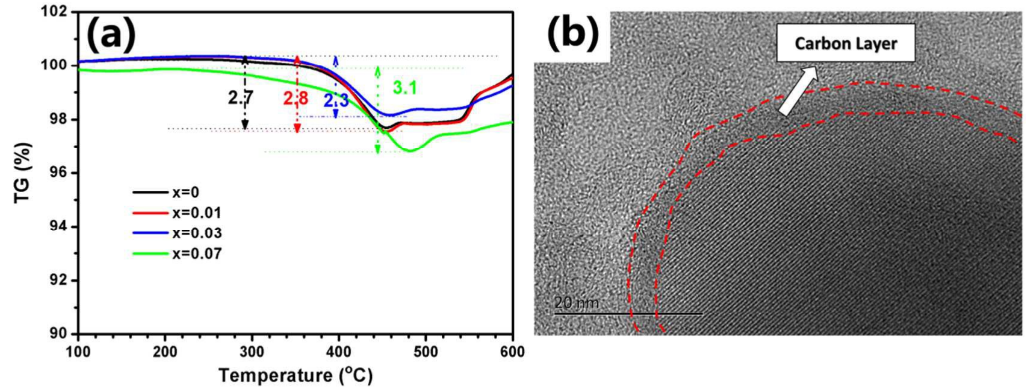
(a)
TG (%)
Temperature (°C)
102
100
98
96
94
92
90
100
200
300
400
500
600
2.7
2.8
2.3
3.1
x=0
x=0.01
x=0.03
x=0.07
(b)
Carbon Layer
20 nm

Figure 4

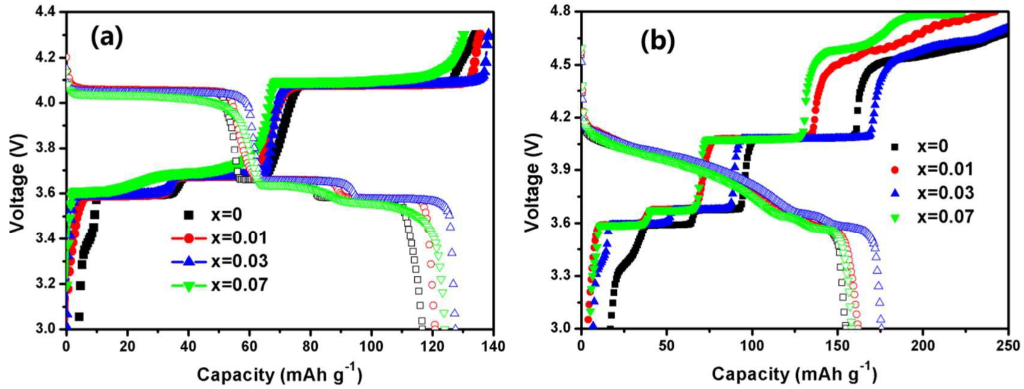
(a)
Voltage (V)
Capacity (mAh g^{-1})
x=0
x=0.01
x=0.03
x=0.07
4.4
4.2
4.0
3.8
3.6
3.4
3.2
3.0
0
20
40
60
80
100
120
140
(b)
Voltage (V)
Capacity (mAh g^{-1})
x=0
x=0.01
x=0.03
x=0.07
4.8
4.5
4.2
3.9
3.6
3.3
3.0
0
50
100
150
200
250

Figure 5

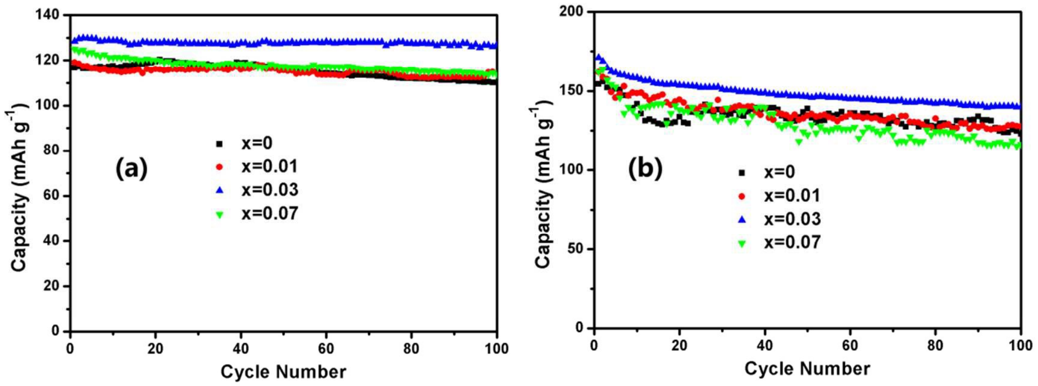
(a)
Capacity (mAh g^{-1})
Cycle Number
0
20
40
60
80
100
120
140
0
20
40
60
80
100
■ x=0
● x=0.01
▲ x=0.03
▼ x=0.07
(b)
Capacity (mAh g^{-1})
Cycle Number
0
50
100
150
200
0
20
40
60
80
100
■ x=0
● x=0.01
▲ x=0.03
▼ x=0.07

Figure 6

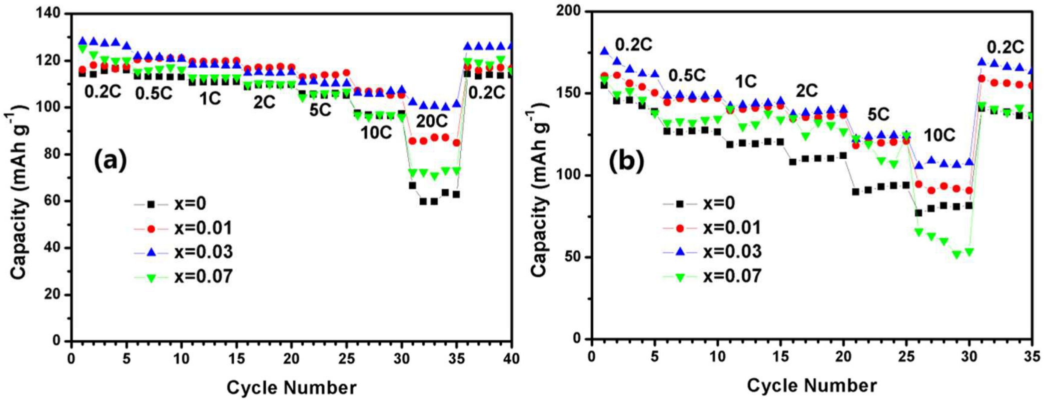
(a)
Capacity (mAh g^{-1})
Cycle Number
0.2C
0.5C
1C
2C
5C
10C
20C
0.2C
x=0
x=0.01
x=0.03
x=0.07
0
20
40
60
80
100
120
140
0
5
10
15
20
25
30
35
40
(b)
Capacity (mAh g^{-1})
Cycle Number
0.2C
0.5C
1C
2C
5C
10C
0.2C
x=0
x=0.01
x=0.03
x=0.07
0
50
100
150
200
0
5
10
15
20
25
30
35

Figure 7

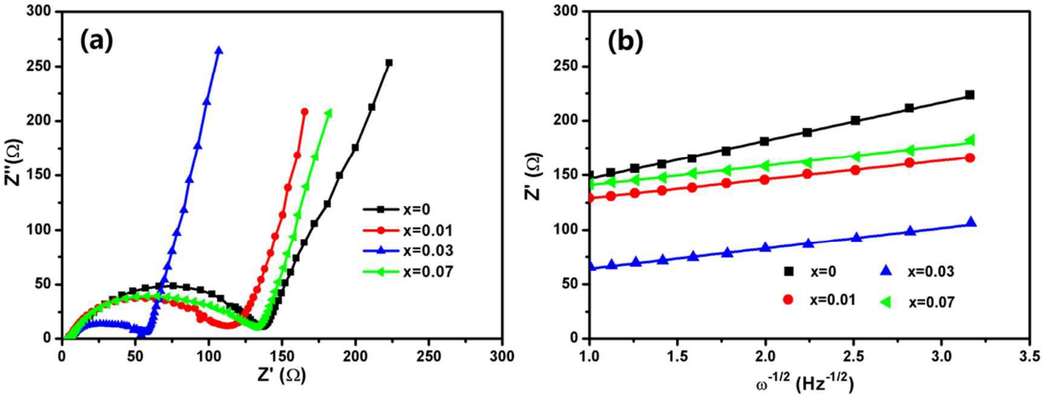
(a)
Z''(Ω)
Z' (Ω)
300
250
200
150
100
50
0
0
50
100
150
200
250
300
x=0
x=0.01
x=0.03
x=0.07
(b)
Z' (Ω)
$\omega^{-1/2}$ (Hz$^{-1/2}$)
1.0
1.5
2.0
2.5
3.0
3.5
x=0
x=0.01
x=0.03
x=0.07

Figure 8

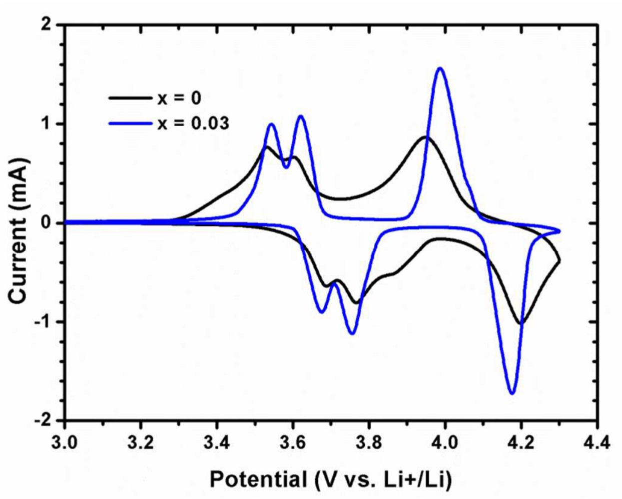
x = 0
x = 0.03
Current (mA)
Potential (V vs. Li+/Li)
2
1
0
-1
-2
3.0
3.2
3.4
3.6
3.8
4.0
4.2
4.4

A Table of Contents Entry

A promising cathode material $Li_3V_2(P_{1-x}B_xO_4)_3/C$ for high-power Li rechargeable batteries shows excellent electrochemical performance.